Volume 12 | Number 22 | 21 November 2025

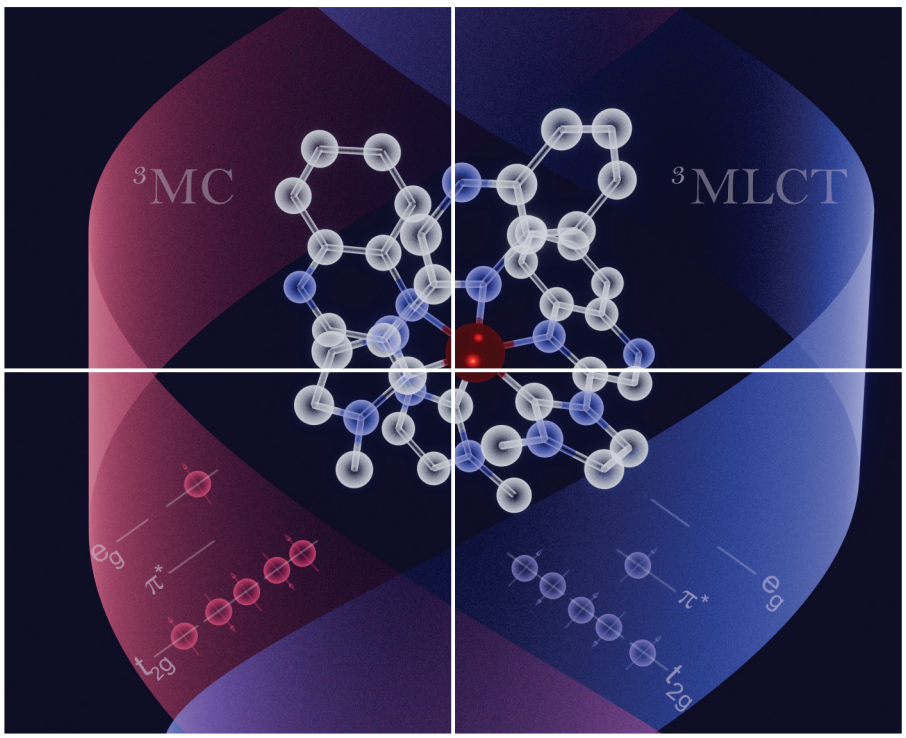

INORGANIC CHEMISTRY

FRONTIERS

CCS 中国化学会 CHINESE CHEMICAL SOCIETY
PEKING UNIVERSITY 1898
ROYAL SOCIETY OF CHEMISTRY
rsc.li/frontiers-inorganic

INORGANIC CHEMISTRY
FRONTIERS

RESEARCH ARTICLE

View Article Online
View Journal | View Issue

Cite this: *Inorg. Chem. Front.*, 2025, **12**, 6946

Fe(II) bidentate complexes with long-lived triplet states

Ulises Carrillo,[a] Ronan Viel,[b] Salwa Simona Jamil,[a] Florian Molton,[c] Carole Duboc,[c] J. Luis Perez-Lustres,[d] Karsten Heyne,[d] Stefan Haacke,*[b] Cristina Cebrian*[e] and Philippe C. Gros*[a,c]

Received 9th May 2025,
Accepted 26th August 2025

DOI: 10.1039/d5qi01105a

rsc.li/frontiers-inorganic

A series of bidentate quinoline/quinoxaline-NHC ligands were coordinated to an iron(II) metal centre with the aim of taking advantage of the combined effect of NHC σ-donor and quinoline/quinoxaline π-acceptors on the excited-state stabilization of the resulting Fe(II) complexes. Excitation of these complexes at 530 nm promoted excited state formation with lifetimes of up to 74 ps. A detailed study combining spectroelectrochemistry, UV/VIS transient absorption spectroscopy as well as steady-state and time-resolved luminescence concludes that these long-lived triplet states display spectroscopic properties compatible with both MC and MLCT character, with a degree of mixing that depends on the precise ligand structure.

Introduction

The development of photoactive complexes from earth-abundant metals is nowadays a hot topic in the course of more sustainable light-responsive materials.[1,2] Recent impressive progress has been made in improving the challenging photophysics of typical polypyridine iron complexes. A judicious tridentate ligand design with specific electronic properties – ranging from N-heterocyclic carbenes (NHC),[3] cyclometallating units[4,5] with the aim to strengthen the ligand field, or the structural rigidity[6] – led to an impressive increase in the MLCT or LMCT lifetime of the corresponding iron complexes up to the ns scale.[7,8]

The increase of the ligand-field splitting can be also promoted by reducing the angular strain around the metal centre ideally adopting the octahedral geometry. Our group has made significant progress in this field by designing bidentate pyridyl-NHC Fe(II) complexes with excited state lifetimes similar to those of their tridentate analogues, while reducing the number of NHC units.[9] The asymmetry of the ligands led expectedly to geometrical isomers. The coordination of pyridine-imidazol-2-ylidene ligand led to an inseparable mixture of *fac*/*mer* isomers (1 : 14 ratio).[10] TD-DFT was thus used to model the excited state properties of both isomers and revealed that, upon excitation, the facial configuration leads to the slowest relaxation kinetics, resulting in longer excited state lifetimes.[11] We focused our efforts on accessing selectively both facial and meridional isomers in azine-NHC Fe(II) complexes by playing with the nature and position of substituents on the azine unit.[12] For example, a methyl group or a chlorine atom alpha to the nitrogen resulted exclusively in a *fac* configuration. In the case of the bulky mesitylene group, target complexes could be obtained only by shifting the steric hindrance to position 5 of the azine producing *mer* isomers instead.

In addition, the π-extended 2-quinoline and 2-quinoxaline groups showed a strong preference for facial isomerism. In addition to this *fac* control, the use of π-extended azines is particularly relevant due to their low-lying MLCT manifold, which results in better absorption in the visible range. Furthermore, the possible weaker electronic coupling with metal-centred states could possibly contribute to longer-lived MLCT triplet states. Herein we report the synthesis of a family of Fe(II) quinoline/quinoxaline NHC complexes (Scheme 1) and investigation of their photophysical and (spectro)electrochemical properties. A peculiar relaxation scenario is proposed leading to long-lived excited states in the 60–74 ps range with a marked mixed ^{3}MC/^{3}MLCT character.

Results and discussion

Synthesis of complexes

Complexes *fac*-**C1** and *fac*-**C2** were prepared as reported before.[12] Complex *fac*-**C3** was obtained in 37% yield from the preligand **HL3**. The preligand **HL4** bearing the isoquinoline

[a]*Université de Lorraine, CNRS, L2CM, 54000 Nancy, France*
[b]*Université de Strasbourg, CNRS, IPCMS, 67000 Strasbourg, France*
[c]*Université de Grenoble Alpes, CNRS, DCM, 38058 Grenoble, France*
[d]*Institut für Experimental-Physik, Freie Universität, Berlin, Germany*
[e]*Université de Strasbourg, CNRS, ICS, 67000 Strasbourg, France*

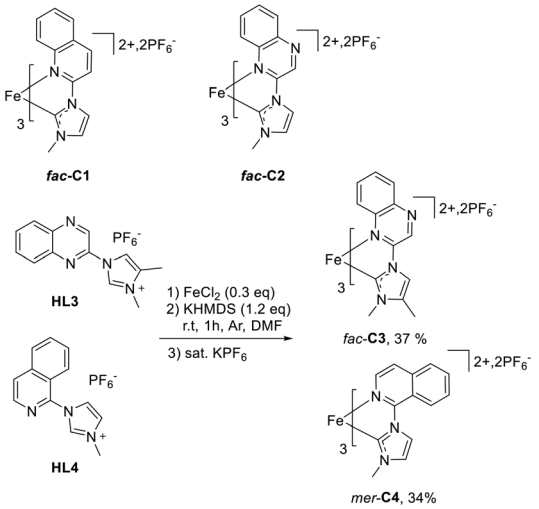

Scheme 1 Complexes studied in this work and the synthesis of *fac*-**C3** and *mer*-**C4**.

led to complex **C4** in 34% yield, mainly in its *mer* form (8 : 92 *fac* : *mer* ratio as determined by ^{1}H NMR), in agreement with the selectivity obtained previously introducing a bulky group at position 5 of the pyridine.[12]

Ground-state characterization

UV-VIS spectroscopy. The UV-VIS absorption spectra of the four complexes in deaerated acetonitrile solution are shown in Fig. 1 and the data are collected in Table 1. The spectra of all complexes present three main absorption bands. The intense bands below 320 nm correspond to $^1(\pi \rightarrow \pi^*)$ ligand-centered transitions. At lower energies, two distinct, broader and less intense MLCT bands correspond to Fe-carbene $^1(d \rightarrow \pi^*NHC)$ transitions (350–420 nm) and Fe-azine $^1(d \rightarrow \pi^*azine)$ transitions, which extend well into the visible region (380–700 nm). However, several differences can be distinguished arising from the ligands' configuration.

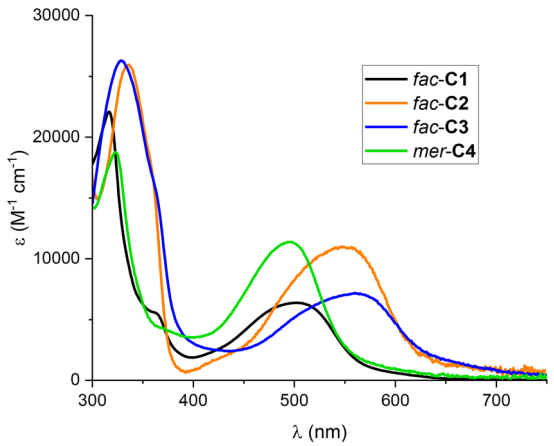

Fig. 1 UV-VIS spectra of the complexes in acetonitrile solutions.

Table 1 Spectroscopic and electrochemical properties of complexes

Complex	λ_{max} (nm) (ε (M^{-1} cm^{-1}))	$E^{ox}_{1/2}$ (Fe^{II}/Fe^{III}) (V *vs.* SCE)	E^{red1}_{pc} (V *vs.* SCE)	ΔE^b (V)
fac-**C1** [12]	317 [22 077] 367 [5157] 504 [6387]	0.78 (97 mV)^a	−1.43	2.25
fac-**C2** [12]	336 [25 976] 428 [1916] 554 [10 904]	1.06 (92 mV)^a	−1.00	2.11
fac-**C3**	329 [26 279] 363 [16 001] 562 [7169]	1.06 (96 mV)^a	−1.00	2.11
mer-**C4**	323 [18 675] 371 [4202] 493 [11 357]	0.69 (86 mV)^a	−1.61	2.34

^{a} $E^{ox}_{pa} - E^{ox}_{pc}$. ^{b} $E^{ox}_{pa} - E^{red1}_{pc}$.

As for the *fac* series, a red-shift of 1790 cm^{-1} of the lowest energy MLCT band is promoted by switching from the quinoline (*fac*-**C1**) to the more π-deficient quinoxaline (*fac*-**C2**) unit. Replacing imidazolylidene with 4-methylimidazolylidene contributed to further lowering the energy of the MLCT band, which is spotted at 562 nm in *fac*-**C3**. The consequence of introducing isoquinoline (*mer*-**C4**) as the central azine is a notable blue shift of the MLCT band by comparison with the quinoxaline series. The MLCT in *mer*-**C4** is found in the same energy domain as the *fac*-**C1** quinoline-based complex, albeit with a nearly twofold increase in band intensity.

Electrochemistry. The redox properties of all complexes were investigated through cyclic voltammetry experiments (CVs) and the main results are summarized in Table 1. As an example, the CV of *fac*-**C2** recorded in MeCN is shown in Fig. 2 (see Fig. S9–11 for other complexes). All the complexes display reversible Fe^{II}/Fe^{III} oxidations in most cases with potentials

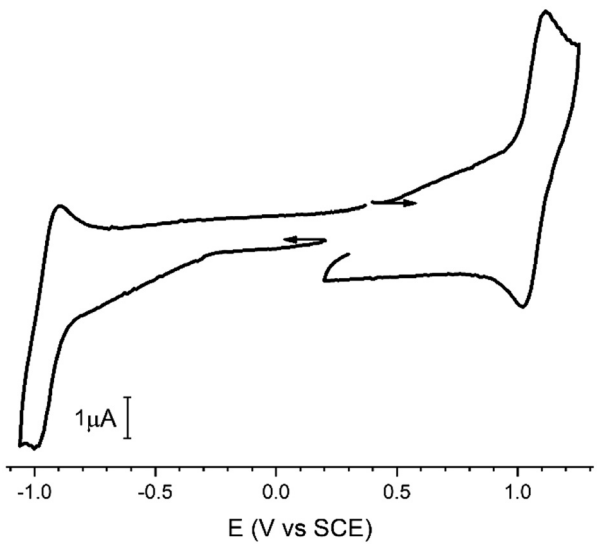

Fig. 2 Cyclic voltammogram of *fac*-**C2** (0.2 mM) in an MeCN solution containing 0.1 M $TBAPF_6$, recorded at v = 100 mV s^{-1}.

ranging 0.69–1.06 V *vs*. SCE (Table 1). These values can be nicely correlated to the π-back donation of Fe(II) to both NHC and azine moieties, which results in higher oxidation potentials due to the stabilization of the t2g-like orbital (HOMO). The potentials of 0.78 V in *fac*-**C1** (quinoline) and 0.69 V in *mer*-**C4** jumped to 1.06 V for *fac*-**C2** (quinoxaline) and *fac*-**C3** combining quinoxaline and 4-methylimidazolylidene.

On the cathodic side, remarkable differences were obtained as well by comparing the first reduction potentials. Drastic cathodic shifts were observed going from *fac*-**C1** (−1.43 V) to both *fac*-**C2** and *fac*-**C3** (−1.00 V) in good agreement with the increased acceptor character and thus, lower energy π* orbitals.

Spectroelectrochemistry (SEC). The one-electron reduced and oxidized species of *fac*-**C2** were electrogenerated to enable their identification *via* UV-VIS and EPR spectroscopy, with the specific aim of determining whether the redox processes are ligand- or metal-centered. The UV-VIS spectroelectrochemical (SEC) measurements performed under an applied anodic potential of 1.2 V *vs.* SCE (Fig. 3(a) for *fac*-**C2**; see Fig. S12–15 for the other three complexes) reveal a rapid evolution of the absorption spectrum during electrolysis. The initial complex, characterized by two main absorption bands at 336 nm and 554 nm, is progressively converted into a new species displaying transitions at 355 nm and 690 nm. The presence of well-defined isosbestic points at 342 nm and 447 nm confirms the clean and complete conversion of *fac*-**C2** into a single oxidized species. Coulometric analysis (0.21 C) further supports a one-electron oxidation process, with one electron transferred per molecule of complex.

Similarly, when a potential of −1.0 V *vs*. SCE is applied, the absorbance spectrum of *fac*-**C2** undergoes a more moderate evolution. The intensity of the main transition at 336 nm decreases, while the band at 554 nm slightly shifts to lower energy. The presence of well-defined isosbestic points at 313 nm, 368 nm, 496 nm, and 567 nm indicated a clean conversion. Coulometry analysis (0.26 C) confirms that the reduction involves the transfer of a single electron per molecule of complex. When the applied potential is returned to its initial value, the original UV-vis spectrum is fully restored in both cases, confirming the reversibility of the oxidation and reduction processes (see Fig. S15).

Unfortunately, the one-electron reduced species of *mer*-**C4** is unstable. As observed with other structurally-related ligands,[13,14] the hydrogen–hydrogen repulsions between the isoquinoline and imidazolylidene moieties may disrupt ligand planarity, thus slightly weakening the metal–ligand bonds. We hypothesized that this steric interaction may be at the origin of the lack of robustness of the reduced species.

X-band cw-EPR experiments were carried out to determine the oxidation and reduction sites (Fig. 4 for complex *fac*-**C2** and Fig. S16–18 for all complexes). As expected for a diamagnetic low-spin Fe(II) complex, the EPR spectrum of *fac*-**C2** is silent (Fig. 4(a)).

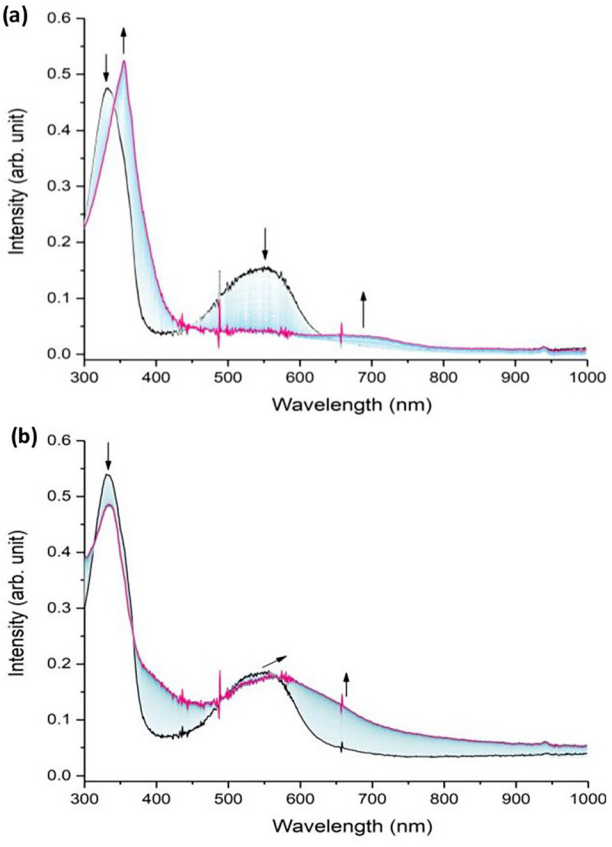

Fig. 3 *In situ* UV-VIS spectra of *fac*-**C2** (0.2 mM) in an acetonitrile solution containing 0.1 M $TBAPF_6$, (a) during exhaustive oxidation at E_{app} = 1.2 V *vs*. SCE (last scan after 285 s), (b) during exhaustive reduction at E_{app} = −1 V *vs*. SCE (last scan after 570 s) (pathlength of 1 mm and scan delay of 5 s between two spectra).

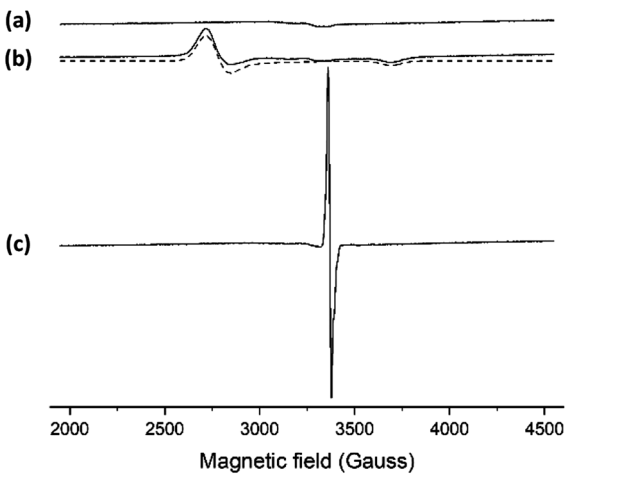

Fig. 4 X-band cw-EPR spectra recorded at 100 K of a MeCN solution of *fac*-**C2** (0.2 mM) containing 0.1 M $TBAPF_6$. (a) Initial Fe(II) complex, (b) after exhaustive electrolysis at E_{app} = 1.2 V *vs*. SCE. Simulation in dashed line for a low-spin S = 1/2 Fe(III) complex with $g_\perp$ = 2.452 and $g_\parallel$ = 1.823, (c) after exhaustive electrolysis at E_{app} = −1 V *vs*. SCE to generate an $Fe(II)L^{\bullet-}$ radical with g = 1.999.

Upon oxidation, the resulting EPR spectrum exhibits an axial signal (Fig. 4(b)). The large anisotropy of the *g*-tensor (Δg = 0.629) in agreement with a low-spin Fe(III) complex (S = 1/2), indicates that the unpaired electron is primarily localized on the Fe centre, evidencing that the oxidation is metal-centred.[15]

In contrast, the EPR spectrum recorded after the electroreduction of *fac*-**C2** (Fig. 4(c)) shows a sharp isotropic feature at g = 2.0023, characteristic of an organic radical, clearly indicating a ligand-centred reduction.

Overall, these SEC experiments demonstrate that the Fe(II) complexes (with the exception of *mer*-**C4**) undergo reversible one-electron oxidation and reduction, leading to the formation of Fe(III) species upon oxidation and radical, ligand-centered Fe(II) species upon reduction.

Excited-state characterization

Transient absorption spectroscopy (TAS). Transient absorption spectra were recorded for all the complexes with excitation at 530 nm. Due to the instability of *mer*-**C4** noticed during SEC experiments, this complex was not subjected to TAS investigations.

Fig. 5 presents a selection of spectra at different time delays, corresponding to complex *fac*-**C2** as well as the ground state absorption in light grey.

The negative signal between 450 nm and 600 nm corresponds to Ground State Bleach (GSB). Ranging from approximately 460 nm to 600 nm, it is in full agreement with the dominating absorption band of the singlet metal-to-ligand charge transfer state (^{1}MLCT) in that region observable in the ground state spectrum.

A smaller bleach feature is also noticeable at wavelengths below 360 nm that correspond to ligand absorption in the steady-state spectrum.

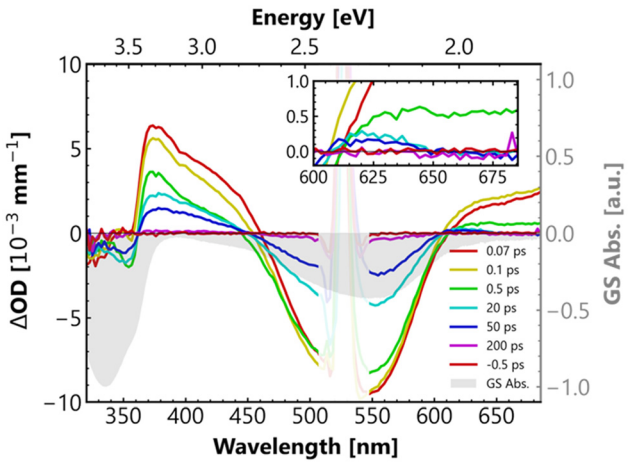

Fig. 5 Selected differential transient absorption spectra of complex *fac*-**C2**. Excitation wavelength 530 nm. The sign-inverted and arbitrarily scaled ground state absorption is plotted for comparison (grey). Inset: zoom into the 600–700 nm region highlighting the narrowing of the red ESA between 0.5 and 20 ps delay.

Two positive bands, corresponding to Excited State Absorption (ESA), can be observed that display different decaying behaviours. The ESA between 360 nm and 450 nm is much stronger and decays on a much longer timescale than the one above 600 nm.

As for a more precise description, in the first 500 fs, the blue ESA undergoes spectral narrowing at longer wavelengths, with a sharp maximum appearing at 380 nm. It then strongly decays before stabilising. In the first 100 fs, no bleach recovery is visible and the red ESA rises. Because of the absence of bleach recovery, the decay of the blue ESA can be assigned to the expected relaxation of ^{1}MLCT into ^{3}MLCT, as is reported in the literature.[9,16–18] On the other hand, the rise of the positive ΔA at λ > 600 nm from 50 to 100 fs is rather due to a reduction of an underlying negative signal at earlier times, as expected for stimulated emission from ^{1}MLCT decaying within <100 fs.

After this first ≈100 fs period, the red ESA continues to decrease, but over two different timescales. On the one hand, for wavelengths above 640 nm, the signal disappears and becomes slightly negative after 10 ps. On the other hand, a small band remains between 600 nm and 640 nm, which fully decays after at least 100 ps (*cf.* inset Fig. 5). This peculiar behaviour is also visible in the blue ESA, yet inverted, since a small region between 360 nm and 400 nm decays in a few picoseconds and smoothens the triangular shape of the strong positive band that finally decays over a longer timescale, in parallel with the decay of the GSB.

In order to further analyse the data, global fitting as well as target analysis have been carried out.

First of all, global analysis reveals 4 time constants that are of respective orders of magnitude of less than 100 fs, less than 1 ps, 10 ps, and 60 ps (see Fig. 6(a)). In fact, the global fit has some difficulty in fitting the kinetics in the red region of the spectrum, where a lifetime of 1 ps to 2 ps seems to match the decays better than a lifetime of 0.6 ps.

Technical considerations aside, the 80 fs lifetime, attributed to ^{1}MLCT decay, is often close to temporal resolution and therefore corresponds to an unresolved component, like in this case (blue line). Its spectrum is also very broad and presents no trace of bleach recovery in the expected region 460–600 nm, as shown by the solid blue line in Fig. 6(a).

The 0.56 ps lifetime mostly contributes to the decay of the broad red ESA, but also with significant negative amplitude to ground state recovery (450–600 nm). However, the relaxation is so fast that vibrational energy cannot be fully dissipated, and the system ends up in what is considered to be a hot ground state GS*. Its assignment arises from the facts that there is ground state recovery with its decay and that its relaxation time of about 10 ps is commonly encountered in literature as the relaxation time for vibrationally excited states.[9,16,17,19–21] Finally, the longest decay time mostly affects the high-energy ESA and contributes the most to ground state recovery compared to the others.

The analysis presented above was carried out on all complexes of the quinoline-based family. They all have quite similar behaviour (Fig. 7), when comparing the decays of com-

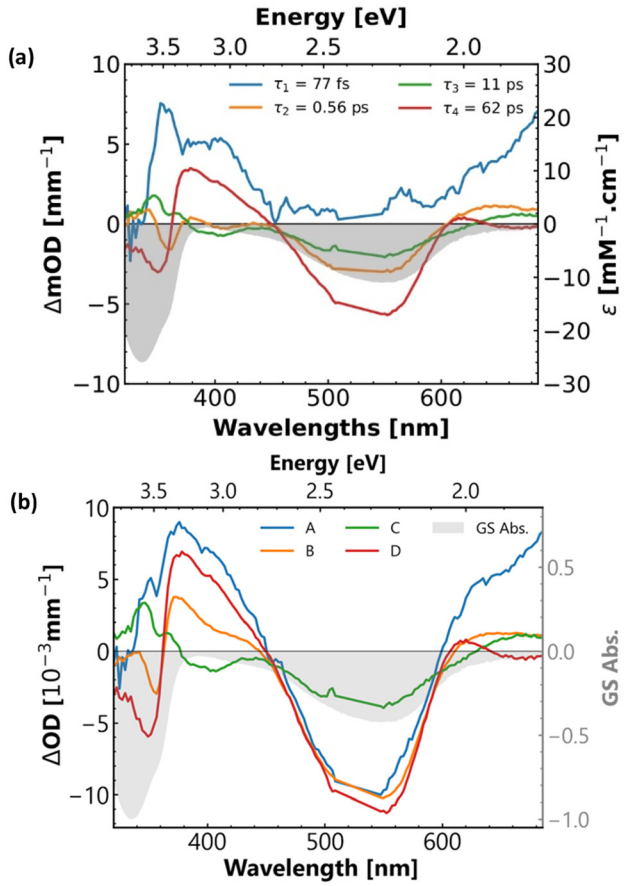

Fig. 6 Decay-associated differential spectra of *fac*-**C2** (a) from global analysis and species-associated spectra (b) of the same complex obtained with the relaxation scheme of Fig. 8.

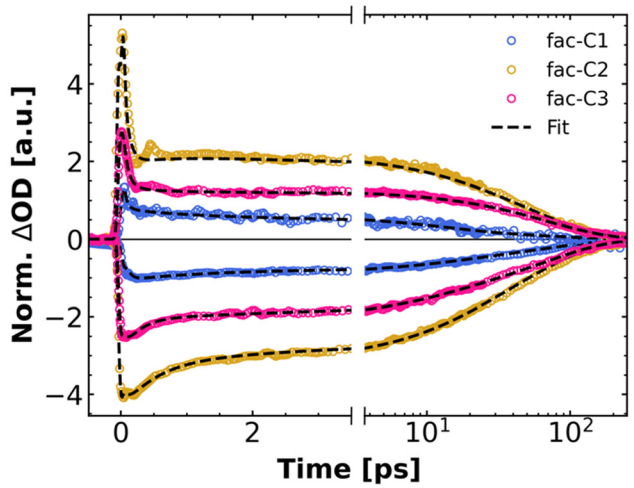

Fig. 7 Comparison of temporal decay traces of complexes *fac*-**C1** (blue), *fac*-**C2** (orange), and *fac*-**C3** (pink). Best fits are represented by black dashed lines. Kinetics were chosen at a maximum of ESA and GSB for all complexes, respectively at 370 nm, 380 nm, and 335 nm (ESA) and 555 nm, 555 nm, and 500 nm (GSB). For the sake of clarity, kinetics were normalised and separated by the application of a scaling factor.

plexes *fac*-**C2**, *fac*-**C3** and *fac*-**C1**. Table 2 summarises the corresponding different lifetimes for all aforementioned complexes.

At first sight, the decaying behaviours of all signals are rather similar, especially for GSB. All complexes present a four-component decay process, with very similar lifetimes.

Because of this resemblance, the analysis performed on complex *fac*-**C2** can be transposed to the other ones. From the DADS, the relaxation scheme shown in Fig. 8 was extracted and further supported by a target analysis (see Fig. 6(b) and section 5.3 of SI).

Target analysis is a method to test different excited state relaxation or reaction scenarios, by calculating the so-called "species-associated spectra" (SADS) as a linear combination of the above DADS.[22] The spectral shapes of the SADS depend on the supposed relaxation scheme, and the most probable relaxation or kinetic scheme is then identified by a critical assessment of the obtained shapes of the SADS.[23] In the SI, we compare the SADS of two reactions schemes (SI, section 8.5). The "parallel model A" assumes that excited state branching occurs from the ^{1}MLCT state into states **B** and **D**, with a 45/55 branching ratio. The "parallel model B" is the one outlined in Fig. 8, where branching occurs with a 50/50 ratio from state **B**, into states **GS*** and **D**, respectively. Excited state branching has been reported for different Fe(II) complexes, with branching occurring mainly from the ^{1}MLCT state,[9,24,25] like assumed here for the "parallel model A".

Table 2 Comparison of the decay times for complexes *fac*-**C1**, *fac*-**C2** and *fac*-**C3** as obtained from global analysis

	fac-**C1**	*fac*-**C2**	*fac*-**C3**
τ_1 [fs]	65	77	60
τ_2 [ps]	0.97	0.56	0.24
τ_3 [ps]	12	11	10
τ_4 [ps]	74	64	71

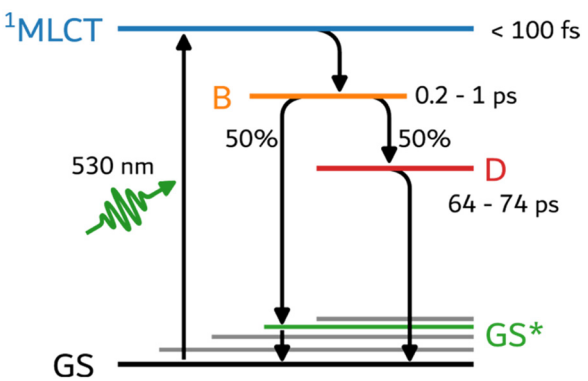

Fig. 8 Proposed relaxation scheme for the family of complexes. The ^{1}MLCT is populated and depleted within less than 100 fs. Its depopulation corresponds to the population of state **B** that decays over the ps timescale into a hot ground state GS* and the long-living state **D**.

But, the "parallel model A" produces a SADS for state **B**, which is not consistent with the evolution of the raw data (Fig. 5), in particular regarding the ESA decay in the 380–440 nm range, between 0.1 and 0.5 ps (**B** has a 0.56 ps lifetime). Indeed, the SADS of state **B** in that model is negative in that spectral range (Fig. S28), and not positive as required for an ESA. On the other hand, the SADS obtained in the "parallel model B" has the correct shape in that frequency range (Fig. S29), which is the main argument for validating this reaction scheme. Note that the spectral shapes of the SADS depend only marginally on the precise branching ratio, meaning that the 50% value is only indicative.

According to the "parallel model B" (Fig. 8), the ^{1}MLCT is populated upon excitation and decays within a very short time to state **B**. The latter lasts for about 1 ps, depending on the complex, and its population is split and decays to the hot ground state GS* and state **D**, decaying with 10–12 ps and 64–74 ps respectively. See Table S1 for the detailed lifetimes of all the complexes.

While TAS experiments performed above allowed the determination of a possible relaxation path, they do not give access to the very nature of states **B** and **D**. The remaining hot question is therefore: which state corresponds to the ^{3}MLCT?

Brown *et al.*, reported that SEC can give a qualitative insight of what the differential absorption of the MLCT triplet state looks like, provided one uses an empirical scaling factor η to enhance the match between SEC and TAS.[26] The scaling factor accounts for differences in the SEC and TAS experiments, such as the molar concentration, the degree of reduction or oxidation in SEC, α_{red} and α_{ox}, and most importantly the percentage of excited Fe(II) complexes in the TAS experiments, R, which determines the amplitude of the ΔA spectra.

Even though α_{red} and α_{ox} are close to one in the SEC experiments, we used our implementation, in which the oxidised and reduced spectra have their own scaling factor, since it offers more flexibility for fitting the TAS difference spectra (see section 6 of the SI for more details).

Fig. 9 presents the differences of the absorption spectra of complex *fac*-**C2** in its oxidised-minus-ground state and reduced-minus-ground state forms, as obtained from SEC (Fig. 3) with $\alpha_{red} = \alpha_{ox} = 1$, as well as a comparison with the SADS of states **B** and **D**, as obtained by target analysis. At a first glance, the agreement of the SADS of both states is good in the 380–450 nm range ($\Delta A > 0$), and better for state **B** in the red (>600 nm). In the bleach region, however ($\Delta A < 0$), the spectra derived from SEC have surprisingly ≈3 times lower amplitude than the SADS of states **B** and **D**. We refer the reader to ref. 26 for a discussion of a variety of reasons explaining why the comparison of differential SEC reference spectra with the ones of non-equilibrated transient TAS species has to remain inevitably on a qualitative level.

With this in mind, a closer inspection of the SEC difference spectra, it appears that the low-energy ESA band (>600 nm) mainly arises from the reduced ligand's absorption. On the other hand, the high-energy ESA is more even in terms of contributions: its high-energy band (370–400 nm) can be considered as a signature of the oxidised metal centre, but the band ranging from 400 nm to 450 nm is quite equilibrated between both species. In the end, with the SEC insight, the short-lived state **B** can be confidently considered as being fully ^{3}MLCT since it bears both features of the oxidised metal and reduced ligand. To determine which type of ligand is the reduced one is unfortunately not possible at this stage. Being able to distinguish the absorption of the reduced carbene and the reduced azine moieties would have allowed to sharpen the analysis.

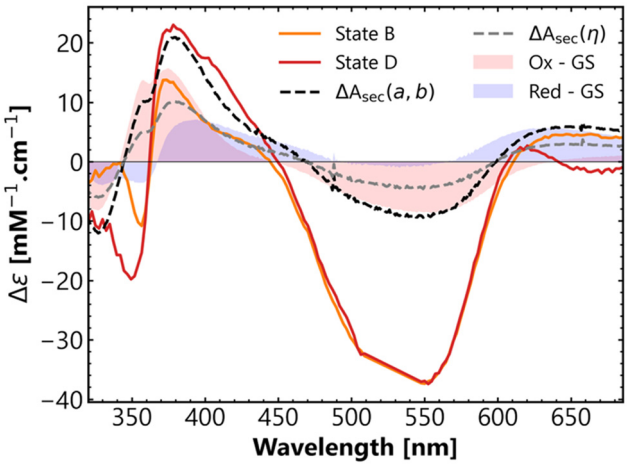

Fig. 9 Difference absorption spectra of complex *fac*-**C2** in oxidised-minus-ground state (red) and reduced-minus-ground state (blue) forms. The solid lines correspond to the species-associated difference spectra of states **B** and **D** (SADS, orange and red). Dashed lines refer to simulations of the differential spectrum of an MLCT-equivalent state, computed either by the approach of ref. 26 (grey dashed) or by the formulas developed in section 6 of the SI (black dashed line). Note that $\alpha_{red} = \alpha_{ox} = 1$ was used for the latter.

Regarding the long-lived excited state **D**, it presents only a small absorption between 600 and 640 nm, in contrast to the absorption of the fully reduced state of the ligand (Fig. 9), and in contrast to expectations for a charge transfer state with a ligand-centred charge. However, the near-UV part (300–380 nm) of its SADS resembles that of the ΔA spectrum of the MLCT state derived from SEC. This observation and the weak reduced-ligand-like positive ΔA at 620 nm support the idea that the initially fully reduced ligand (states **A** and **B**) is still partially reduced during the lifetime of state **D**.

Steady-state and time-resolved luminescence spectroscopy. To complete the study, steady-state and time-resolved luminescence measurements were carried out for the three complexes. We focus here on the results of *fac*-**C2** again as an example. Even though a luminescence quantum yield $<10^{-4}$ can be anticipated for the above identified triplet state character of state **D**, we were able to detect a weak steady-state emission and corresponding excitation spectra as reported in the SI (Fig. S21). As detailed there, the luminescence is due to two different species or transitions, with a large spectral overlap. Using a highly sensitive Hamamatsu streak camera with 10 ps

resolution (see exp. details below), we separate the two emission components according to their respective decay times, and spectra (DAS).

Fig. 10a reports the wavelength-resolved kinetic traces for complex *fac*-**C2** (*cf.* Fig. S22 & S23 for the complete data set). For shorter wavelengths (550 and 600 nm), the kinetic traces show an unresolved peak at t = 0, most likely due to bright sub-ps emission from the ^{1}MLCT singlet state. At longer times, the curved slope of the plots, displayed on a logarithmic y-axis, indicate multi-exponential decays, the analysis of which is summarized in the different decay-associated spectra (DAS) obtained by a global analysis in Fig. 10(b). The most interesting result here is the presence of a 56 ps lifetime, which agrees with the lifetime of state **D** as obtained by TAS (64 ps), and which is directly evident in the kinetic trace at 725 nm, dominating the decay in the first 150 ps (Fig. 10(a)). For the longer decay times, the fit gives a 430 ps and a >1 ns component, indicated as "infinity" in Fig. 10(a). As compared to the DAS of the slower decay times, the one of 56 ps is markedly different, first because of its lower amplitude and second because of its flatter and broader shape, especially towards longer wavelengths in the near-IR region.

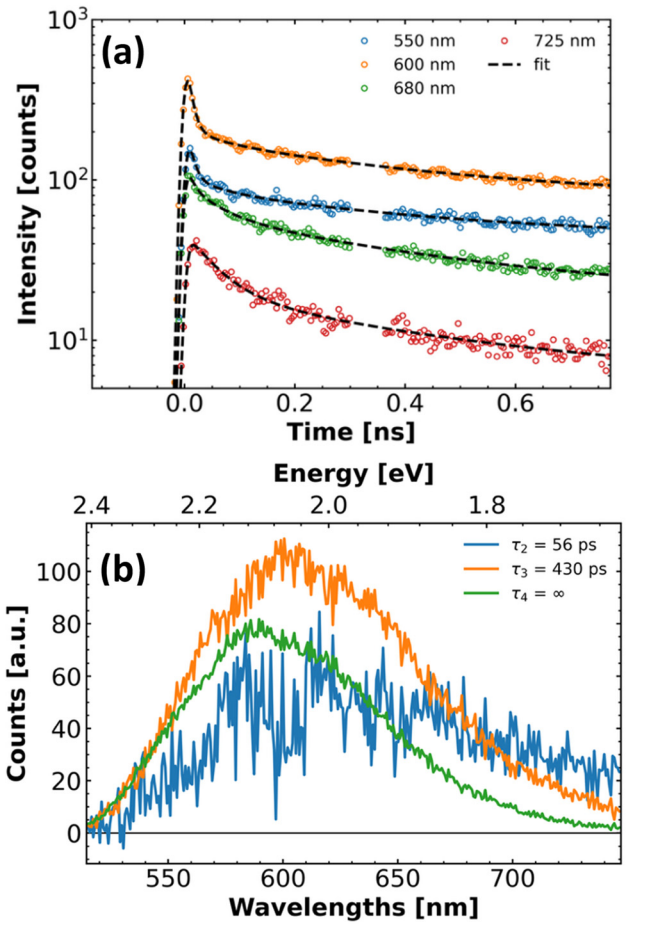

Fig. 10 Time-resolved emission data of *fac*-**C2** recorded with a streak camera (10 ps time resolution FHWM). Excitation with 0.3 ps pulses at 515 nm, and detection through a long-pass OG550 filter. (a) Kinetic traces of the time-dependent luminescence measurement with best fits as dashed lines. (b) Decay-associated spectra (DAS) of the different lifetimes found by global analysis.

Regarding the two other DADS, associated with the slower decay times, they appear to be blue-shifted with respect to the one of the triplet state **D**. Hence, the longer-lived emission comes from different states, populated in parallel, much likely arising from a transition or species with small absorption or concentration, hence weakly excited by the 515 nm pulses. Indeed, absorption at 515 nm is dominated by the ^{1}MLCT transition (Fig. 1), and TAS, which reveals only the majority species excited, does display τ_4 = 64 ps with high amplitude (Fig. 6). The slower components found in the luminescence decay (τ_3 and τ_4 in Fig. 10b) appear in TAS as a long-lived, >2 ns lifetime component, with almost zero amplitude (*cf.* sections 8.3 and 8.4 in SI).

Furthermore, as we show in section 7 of the SI, the luminescence excitation and the ground state absorption spectra have largely different shapes. Their comparison indicates that the longer-lived components are indeed due to species of low concentration, possibly (partially) de-coordinated ligands (*cf.* Fig. S21, and related discussion in SI).[27–30]

However, by multiplying the amplitude of the DAS with the corresponding lifetimes, one can estimate that the time-integrated emission of these long-lived species is approximately two orders of magnitude larger than the one of the short-lived triplet state **D**, present in the high concentration *fac*-**C2** complexes. This indicates that the low concentration of the de-coordinated ligands (absence in absorption spectra) is compensated by a relatively high fluorescence quantum yield (≈10%), *i.e.* their emission stems most likely from singlet states.

In the next step, the picosecond luminescence data are used to assess whether state **D** is of MLCT nature as state **B**, or not. To this end, we investigated the radiative decays of the iron complexes and compared them with respect to the standard $[Ru(bpy)_3]^{2+}$, and used the following approach in order to compare their radiative rates k_r. The population of state **D** or of the ^{3}MLCT state in $[Ru(bpy)_3]^{2+}$ decay according to radiative and non-radiative decay channels with the corresponding rates k_r and k_{nr}:

$$\frac{dN}{dt} = -k_r N(t) - k_{nr} N(t) \quad (1)$$

The first term on the right hand side determines the luminescence intensity $I(t) \propto k_r N(t)$, where the proportionality factor is determined by experimental parameters, such as the luminescence collection efficiency and the detection sensitivity. In particular at "time zero", *i.e.* at the peak of emission

$$I(t=0) \propto k_r N(t=0) \quad (2)$$

since the number of photons emitted per time interval dt is equal to the number of exc. state molecules decaying radiatively.

Experimentally, in the streak camera experiments with a time step of dt = 3 ps, one can assume that $N(t = 0)$ is equal to the number of excited molecules since the non-radiative pro-

Table 3 Summary of the ratios of experimental decay rates of the investigated iron complexes *vs.* $[Ru(bpy)_3]^{2+}$

	fac-**C1**	*fac*-**C2**	*fac*-**C3**
$\bar{k}_{exp}$	2.0	5.1	12.3

The approach has an error bar of typically ±30%.

cesses act on a much slower time scale ($dt \ll 1/k_{nr}$). Hence, the radiative rate can be extracted or compared for different complexes, provided that $N(t = 0)$ is the same. We therefore used exactly the same excitation intensity and corrected for small differences in the absorbances of the different complex solutions.

For a simplified comparison with the radiative rate of $[Ru(bpy)_3]^{2+}$, we use $\bar{k}_{exp}$, defined as the ratio of the time-zero intensities

$$\bar{k}_{exp} = \frac{I(t = 0, \text{Ru})}{I(t = 0, \text{Fe})} = \frac{k_r(\text{Ru})}{k_r(\text{Fe})} \quad (3)$$

as a relative metric to compare the radiative rates of the ruthenium complex to the iron ones, with the results given in Table 3. Note that for the iron complexes $I(t = 0, \text{Fe})$ is the time-zero amplitude of the luminescence component of state **D**, *i.e.* the spectrally integrated DAS related to τ_2 in Fig. 10b.

Due to the well-established Laporte selection rule for d–d transitions, ^{3}MC states are deemed to have a zero radiative rate, but since the present NHC Fe(II) complexes do not obey octahedral symmetry, the Laporte rule does not hold. Nevertheless, based on some rare reports on the extinction coefficients or emission properties of ^{3}MC states in Co(III) complexes,[31,32] one may expect, for the present Fe(II) complexes that $\bar{k}_{exp}$ be >10 or more.

As can be noticed from Table 3, the value of $\bar{k}_{exp}$ strongly depends on the complex. The complex *fac*-**C1** has a radiative rate only twice as low as the ^{3}MLCT state of $[Ru(bpy)_3]^{2+}$, tending to suggest that state **D** of *fac*-**C1** has a strong MLCT character. The same conclusion cannot be drawn as confidently for *fac*-**C3**, with its 12-fold lower radiative rate as compared to $[Ru(bpy)_3]^{2+}$. While according to the literature that reports Fe(II) bidentate complexes' ^{3}MC states with lifetimes of 63 ps or more,[13,33] the logical pathway would label state **D** as ^{3}MC, we could advance here the hypothesis of a mixing between ^{3}MC and ^{3}MLCT states, with proportions depending on the ligand.

Conclusions

A series of Fe(II) quinoline/quinoxaline-NHC complexes was prepared with the aim of studying the impact of σ-donating NHC and π-accepting quinoline/quinoxaline on their excited-state properties.

Thanks to spectroelectrochemistry and transient absorption spectroscopy, a relaxation scheme was drawn where two states, **B** and **D**, were identified to be populated from the ^{1}MLCT state. State **B** is a ^{3}MLCT state, since it displays the characteristic absorption features of the reduced ligands. Independent on the ligand design, its lifetime is only in the 1 ps range. On the other hand, the nature of the long-lived (60–74 ps lifetime) state **D** is difficult to identify clearly, since its spectroscopic features are compatible with both an MLCT and MC character. Indeed, state **D** shows absorption features of the reduced ligand, as expected for the ligand-centred triplet, but only in the near-UV/blue and in the red part of the spectrum. In addition, time-resolved luminescence experiments show, for two of the three complexes, that state **D** has a radiative rate lower than, but in the same order of magnitude as, the one of the ^{3}MLCT state of $[Ru(bpy)_3]^{2+}$. Surely, we cannot expect a zero-dipole moment or radiative rate for an ^{3}MC state in these bidentate heterocyclic complexes, since Laporte's rule does only hold for a perfect octahedral symmetry. Rather, the different spectroscopic properties probed here by steady-state, ultrafast luminescence and absorption spectroscopy suggest that state **D** is a mixture of ^{3}MC and ^{3}MLCT character, with the relative proportion depending on the precise ligand. In other words, we hypothesize that the molecular orbital of excited state **D** covers both the metal centre and one of the ligands, hence a mixed MC- and MLCT-character. This motivates the observation of excited state absorption features, which resemble the ones of reduced ligands in shape and amplitude. But, it would be very helpful to have computed excited state spectra for these transient states **D**. Note that the concept of such states with mixed adiabatic character is ubiquitous and accepted since long, for instance in the simulation of the ground state absorption spectra of iron or other transition metal complexes.[34–39] For the present bi-dentate complexes, this mixed state character will be further investigated and substantiated in our forthcoming publication, reporting on femtosecond vibrational spectroscopy and on TD-DFT simulations of the excited states.

Experimental

Synthesis

Complexes *fac*-**C1** and *fac*-**C2** have been prepared according to ref. 12 *fac*-**C3**. Ligand **HL3** (200 mg, 0.54 mmol) and $FeCl_2$ (22.6 mg, 0.18 mmol) were submitted to three vacuum/Ar cycles, after that 3 mL of dry and degassed DMF were added, the mixture was stirred under Ar at r.t for 5 min then KHMDS (130 mg, 0.65 mmol) were added. The reaction mixture was stirred at r.t. for 1 h. Afterwards, H_2O (10 mL) was added and 1 mL of KPF_6 (saturated solution) the reaction was vigorously stirred and the precipitated formed was filtered in a sintered funnel #3. The solid was washed with H_2O (10 mL) and diethyl ether (3 × 15 mL) until the solid was a fine powder. The solid was recovered by adding acetonitrile and purified by column chromatography using a mixture 10 : 2 : 1 (acetone : water : sat. KNO_3). The recovered fractions were mixed in a balloon and an extra amount of H_2O (3 mL) was added. Acetone was sub-

sequently removed under vacuum and a small quantity of NH_4PF_6 was added until a precipitated appeared. The solid was filtered in a glass funnel filter #4, washed with diethyl ether (3 × 10 mL) and recovered with acetonitrile in a round flask, affording the desired complex *fac*-**C3** in 37% (45 mg) as a reddish solid. ^{1}H NMR (400 MHz, CD_3CN, 298 K) δ 9.3 (s, 1H, H_1), 8.3 (dd, J = 8.4, 1.5 Hz, 1H, H_5), 8.1 (t, J = 1.2 Hz, 1H, H_6), 7.7 (ddd, J = 8.4, 7.0, 1.2 Hz, 1H, H_4), 7.1 (ddd, J = 8.6, 7.0, 1.5 Hz, 1H, H_3), 6.8 (dd, J = 8.7, 1.2 Hz, 1H, H_2), 2.7 (s, 3H, H_8), 2.1 (s, 3H, H_7). ^{13}C{^{1}H} NMR (100 MHz, CD_3CN, 298 K) δ 203.6 (C_1), 149.1 (C_4), 143.2 (C_2), 142.6 (C_{11}), 138.9 (C_6), 136.6 (C_5), 133.4 (C_{10}), 132.4 (C_9), 131.1 (C_7), 123.9 (C_8), 117.1 (C_3), 33.2 (C_{12}), 10.5 (C_{13}). HRMS (ESI-TOF) m/z: $[M - 2PF_6^-]^{2+}$ calcd for $C_{39}H_{36}N_{12}Fe$ 364.1262; found: 364.1291.

mer-**C4**. Ligand **HL4** (200 mg, 0.56 mmol) and $FeCl_2$ (23.6 mg, 0.18 mmol) were submitted to three vacuum/Ar cycles, after that 3 mL of dry and degassed DMF were added, the mixture was stirred under Ar at r.t for 5 min then KHMDS (160 mg, 0.78 mmol) were added. The reaction mixture was stirred at r.t. for 1 h. Afterwards, H_2O (10 mL) was added and 1 mL of KPF_6 (saturated solution) the reaction was vigorously stirred and the precipitated formed was filtered in a sintered funnel #3. The solid was washed with H_2O (10 mL) and diethyl ether (3 × 15 mL) until the solid was a fine powder. The solid was recovered by adding acetonitrile and purified by column chromatography using a mixture 10 : 2 : 1 (acetone : water : $KNO_{3(saturated\ solution)}$). The recovered fractions were mixed in a balloon and an extra amount of H_2O (3 mL) was added. Acetone was subsequently removed under vacuum and a small quantity of NH_4PF_6 was added until a precipitated appeared. The solid was filtered in a glass funnel filter #4, washed with diethyl ether (3 × 10 mL) and recovered with acetonitrile in a round flask, affording the desired complex *mer*-**C4** in 34% (45 mg) as an intense reddish solid in 8 : 92 ratio. ^{1}H NMR (400 MHz, CD_3CN, 300 K) δ 8.8 (d, J = 2.4 Hz, 1H, H_{2mer}), 8.7 (d, J = 2.2 Hz, 1H, H_{2mer}), 8.7 (d, J = 2.3 Hz, 2H, H_{2mer}), 8.7 (d, J = 1.5 Hz, 1H), 8.7–8.6 (m, 1H, H_{8mer}), 8.1–8.0 (m, 1.5H), 8.0 (dt, J = 6.9, 3.5 Hz, 1H), 7.9–7.8 (m, 11H), 7.8–7.7 (m, 1.5H), 7.8 (t, J = 1.1 Hz, 0.4H), 7.7 (d, J = 6.3 Hz, 1H, H_{8mer}), 7.6 (dd, J = 6.4, 0.9 Hz, 1H, H_{7mer}), 7.5 (dd, J = 6.4, 0.9 Hz, 0.4H, H_{7fac}), 7.5 (d, J = 2.3 Hz, 1H, H_{1mer}), 7.4 (d, J = 2.3 Hz, 1H, H_{1mer}), 7.3 (d, J = 2.4 Hz, 1H, H_{1mer}), 7.3–7.2 (m, 2H, H_{7mer} and H_{8mer}), 6.9 (d, J = 6.4 Hz, 0.4H, H_{8fac}), 6.8 (d, J = 6.6 Hz, 1H, H_{7mer}), 3.2 (s, 3H, H_{9mer}), 3.0 (s, 1H, H_{9fac}), 2.7 (s, 3H, H_{9mer}), 2.7 (s, 3H, H_{9mer}). ^{13}C{^{1}H} NMR (100 MHz, CD_3CN, 300 K) δ 212.3 (C_1), 209.7 (C_1), 207.2 (C_1), 146.8, 145.2, 142.5, 139.6, 138.6, 138.2, 133.4, 133.0, 132.7, 130.7, 130.5, 130.4, 129.0, 128.9, 128.8, 128.8, 128.7, 124.0, 123.2, 123.1, 122.8, 122.7, 121.7, 121.3, 121.3, 120.7, 120.6, 119.9, 119.8, 37.4, 37.2 (C_2), 36.5 (C_2), 36.3 (C_2). HRMS (ESI-TOF) m/z: $[M - 2PF_6^-]^{2+}$ calcd for $C_{39}H_{33}N_9Fe$ 341.6099; found: 341.6099.

Transient absorption spectroscopy

All complexes have been excited at 530 nm where they present a common acceptable absorption level. The samples were prepared in commercial acetonitrile such that their optical density at the excitation wavelength lies between 0.5 and 0.7 mm^{-1} in a 1 mm quartz cuvette.

About the setup: a 800 nm pulsed beam with 5 kHz repetition rate is generated by pumping a Ti:sapphire crystal. Mode-locking is then used to obtain laser pulses, of about 40 fs duration. After chirped pulse amplification, the beam is split into two paths. On the one hand, it is used to generate the pump with a commercial OPA (TOPAS from light conversion); after the TOPAS, pulse duration is about 80 fs. On the other hand, the 800 nm beam is focused into either a CaF_2 or a sapphire crystal depending on whether one wants to probe in the near UV or in NIR.

Complexes were excited with pump at magic angle (54.7°) and 700 μW power, *i.e.* 1.4 mJ cm^{-2} energy density per pulse at 5 kHz repetition rate and with 100 μm FWHM beam diameter at pump–probe spatial overlap.

Steady state and time-resolved luminescence

The steady-state luminescence emission and excitation spectra were recorded on a Horiba/Jobin Yvon Fluorolog spectrometer. In order to record spectra with a good signal-to-noise ratio, slit widths of "5 nm" were used for both excitation and detection, and up to 20 spectral scans were averaged. The influence of reflected or scattered excitation light was minimised by a proper orientation of the 1 mm sample cuvettes. No bandpass or low-pass filter was used. The standard correction factors were applied both for the spectral sensitivity of detectors and for the wavelength-dependent intensity of the Xe lamp (excitation spectra).

For the picosecond luminescence measurements, the data were recorded with a Hamamatsu C10627 time-gated streak camera (10 ps FWHM time resolution). All complexes were excited at 515 nm after frequency doubling of the 1030 nm output of an Yb:fiber laser (Tsunami, Amplitude) at 10 kHz repetition rate and with 1.0 mW average power per pulse. With 100 μm FWHM diameter at the focal point, the energy density was 1 mJ cm^{-2}. An OG550 low-pass filter (Schott Glass) was used.

In order to have similar experimental conditions for all complexes (iron and ruthenium), the ruthenium solution was highly concentrated (2.5 mM) to reach an optical density of 0.5 mm^{-1} at 515 nm.

Spectroelectrochemistry

Electrochemistry was performed on a Metrohm Autolab PGStat100 potentiostat using a conventional three-electrode cell in glove box under argon atmosphere. Complexes were dissolved at 0.2 mM in acetonitrile containing 0.1 M Bu_4NPF_6 as supporting electrolyte. The reference electrode was Ag/Ag^+ in electrolytic solution ($AgNO_3$ 10 mM) and the counter-electrode was a platinum wire. The working electrode was a commercial 3 mm-diameter glassy carbon disk for cyclic voltammetry, and a glassy carbon foam (of around 0.4 cm^3 and 80 ppi) for bulk electrolysis. All potentials were converted *vs.* SCE by E(*vs.* SCE) = E(*vs.* Ag/Ag^+) + 0.298 V. In all the experiments the scan rate was 100 mV s^{-1}. *In situ* UV-visible spectrometry was performed

with a xenon lamp and a Avaspec detector from Avantes connected by optical fibers to a Hellma immersion probe with a pathlength of 1 mm.

X-band EPR spectra were recorded at 100 K with a EMX Plus Bruker spectrometer equipped with a ER4119HS Bruker cavity. All spectra presented were recorded under non-saturating conditions. EPR spectral simulation was carried out using the Easyspin program.[40]

Author contributions

U. C. and S. S. J. performed the synthesis and ground state characterizations of ligands and complexes. R. V. performed TAS experiments and analysed the results with J. L. P. L., K. H. and S. H. F. M. performed SEC and EPR experiments and analysed the results with C. D., P. C. G. and C. C. conceived the project and wrote the manuscript with C. D., R. V. and S. H.

Conflicts of interest

There are no conflicts to declare.

Data availability

The data supporting this article have been included as part of the SI. See DOI: **https://doi.org/10.1039/d5qi01105a**.

Acknowledgements

The authors thank the SunHy ANR project (ANR 21-CE50-0040) for grants to S. S. J. and R. V. The Nano-Bio ICMG (UAR 2607) is acknowledged for providing facilities for EPR analyses.

References

1 O. S. Wenger, Photoactive Complexes with Earth-Abundant Metals, *J. Am. Chem. Soc.*, 2018, **140**(42), 13522–13533, DOI: **10.1021/jacs.8b08822**.

2 M. Pastore, S. Caramori and P. C. Gros, Iron-Sensitized Solar Cells (FeSSCs), *Acc. Chem. Res.*, 2024, **57**(4), 439–449, DOI: **10.1021/acs.accounts.3c00613**.

3 K. S. Kjær, N. Kaul, O. Prakash, P. Chábera, N. W. Rosemann, A. Honarfar, O. Gordivska, L. A. Fredin, K.-E. Bergquist, L. Häggström, T. Ericsson, L. Lindh, A. Yartsev, S. Styring, P. Huang, J. Uhlig, J. Bendix, D. Strand, V. Sundström, P. Persson, R. Lomoth and K. Wärnmark, Luminescence and Reactivity of a Charge-Transfer Excited Iron Complex with Nanosecond Lifetime, *Science*, 2019, **363**(6424), 249–253, DOI: **10.1126/science.aau7160**.

4 J. Steube, A. Kruse, O. S. Bokareva, T. Reuter, S. Demeshko, R. Schoch, M. A. Argüello Cordero, A. Krishna, S. Hohloch, F. Meyer, K. Heinze, O. Kühn, S. Lochbrunner and M. Bauer, Janus-Type Emission from a Cyclometalated Iron (III) Complex, *Nat. Chem.*, 2023, **15**(4), 468–474, DOI: **10.1038/s41557-023-01137-w**.

5 W. Leis, M. A. Argüello Cordero, S. Lochbrunner, H. Schubert and A. Berkefeld, A Photoreactive Iron(II) Complex Luminophore, *J. Am. Chem. Soc.*, 2022, **144**(3), 1169–1173, DOI: **10.1021/jacs.1c13083**.

6 J. T. Malme, R. A. Clendening, R. Ash, T. Curry, T. Ren and J. Vura-Weis, Nanosecond Metal-to-Ligand Charge-Transfer State in an Fe(II) Chromophore: Lifetime Enhancement via Nested Potentials, *J. Am. Chem. Soc.*, 2023, **145**(11), 6029–6034, DOI: **10.1021/jacs.2c13532**.

7 L. Lindh, P. Chábera, N. W. Rosemann, J. Uhlig, K. Wärnmark, A. Yartsev, V. Sundström and P. Persson, Photophysics and Photochemistry of Iron Carbene Complexes for Solar Energy Conversion and Photocatalysis, *Catalysts*, 2020, **10**(3), 315, DOI: **10.3390/catal10030315**.

8 C. Cebrián, M. Pastore, A. Monari, X. Assfeld, P. C. Gros and S. Haacke, Ultrafast Spectroscopy of Fe(II) Complexes Designed for Solar–Energy Conversion: Current Status and Open Questions, *ChemPhysChem*, 2022, **23**(7), e202100659, DOI: **10.1002/cphc.202100659**.

9 K. Magra, A. Francés-Monerris, C. Cebrián, A. Monari, S. Haacke and P. C. Gros, Bidentate Pyridyl–NHC Ligands: Synthesis, Ground and Excited State Properties of Their Iron(II) Complexes and the Role of the Fac/Mer Isomerism, *Eur. J. Inorg. Chem.*, 2022, **2022**(7), e202100818, DOI: **10.1002/ejic.202100818**.

10 A. Francés-Monerris, K. Magra, M. Darari, C. Cebrián, M. Beley, E. Domenichini, S. Haacke, M. Pastore, X. Assfeld, P. C. Gros and A. Monari, Synthesis and Computational Study of a Pyridylcarbene Fe(II) Complex: Unexpected Effects of *Fac*/*Mer* Isomerism in Metal-to-Ligand Triplet Potential Energy Surfaces, *Inorg. Chem.*, 2018, **57**(16), 10431–10441, DOI: **10.1021/acs.inorgchem.8b01695**.

11 A. Francés–Monerris, P. C. Gros, X. Assfeld, A. Monari and M. Pastore, Toward Luminescent Iron Complexes: Unravelling the Photophysics by Computing Potential Energy Surfaces, *ChemPhotoChem*, 2019, **3**(9), 666–683, DOI: **10.1002/cptc.201900100**.

12 U. Carrillo, A. Francés-Monerris, A. R. Marri, C. Cebrián and P. C. Gros, Substituent-Induced Control of *Fac*/*Mer* Isomerism in Azine-NHC Fe(II) Complexes, *ACS Org. Inorg. Au*, 2022, **2**(6), 525–536, DOI: **10.1021/acsorginorgau.2c00038**.

13 R. J. Ortiz, R. Mondal, J. K. McCusker and D. E. Herbert, Leveraging Intramolecular π-Stacking to Access an Exceptionally Long-Lived^3 MC Excited State in an Fe(II) Carbene Complex, *J. Am. Chem. Soc.*, 2025, **147**(2), 1694–1708, DOI: **10.1021/jacs.4c12650**.

14 P.-N. Lai, C. H. Brysacz, M. K. Alam, N. A. Ayoub, T. G. Gray, J. Bao and T. S. Teets, Highly Efficient Red-Emitting Bis-Cyclometalated Iridium Complexes, *J. Am. Chem. Soc.*, 2018, **140**(32), 10198–10207, DOI: **10.1021/jacs.8b04841**.

15 J.-J. Girerd, M.-L. Boillot, G. Blain and E. Rivière, An EPR Investigation of the Electronic Structure of Pseudo-Octahedral and Spin Crossover Catecholato-Iron(III) Complexes in the Low-Spin State, *Inorg. Chim. Acta*, 2008, **361**(14–15), 4012–4016, DOI: 10.1016/j.ica.2008.03.077.

16 T. Duchanois, T. Etienne, C. Cebrián, L. Liu, A. Monari, M. Beley, X. Assfeld, S. Haacke and P. C. Gros, An Iron–Based Photosensitizer with Extended Excited–State Lifetime: Photophysical and Photovoltaic Properties, *Eur. J. Inorg. Chem.*, 2015, **2015**(14), 2469–2477, DOI: 10.1002/ejic.201500142.

17 M. Darari, E. Domenichini, A. Francés-Monerris, C. Cebrián, K. Magra, M. Beley, M. Pastore, A. Monari, X. Assfeld, S. Haacke and P. C. Gros, Iron(II) Complexes with Diazinyl-NHC Ligands: Impact of π-Deficiency of the Azine Core on Photophysical Properties, *Dalton Trans.*, 2019, **48**(29), 10915–10926, DOI: 10.1039/C9DT01731C.

18 K. Magra, M. Darari, E. Domenichini, A. Francés-Monerris, C. Cebrián, M. Beley, M. Pastore, A. Monari, X. Assfeld, S. Haacke and P. C. Gros, Photophysical Investigation of Iron(II) Complexes Bearing Bidentate Annulated Isomeric Pyridine-NHC Ligands, *J. Phys. Chem. C*, 2020, **124**(34), 18379–18389, DOI: 10.1021/acs.jpcc.0c03638.

19 L. Liu, T. Duchanois, T. Etienne, A. Monari, M. Beley, X. Assfeld, S. Haacke and P. C. Gros, A New Record Excited State ^{3} MLCT Lifetime for Metalorganic Iron(II) Complexes, *Phys. Chem. Chem. Phys.*, 2016, **18**(18), 12550–12556, DOI: 10.1039/C6CP01418F.

20 K. Magra, M. Darari, E. Domenichini, A. Francés-Monerris, C. Cebrián, M. Beley, M. Pastore, A. Monari, X. Assfeld, S. Haacke and P. C. Gros, Photophysical Investigation of Iron(II) Complexes Bearing Bidentate Annulated Isomeric Pyridine-NHC Ligands, *J. Phys. Chem. C*, 2020, **124**(34), 18379–18389, DOI: 10.1021/acs.jpcc.0c03638.

21 C. Zahn, M. Pastore, J. L. P. Lustres, P. C. Gros, S. Haacke and K. Heyne, Femtosecond Infrared Spectroscopy Resolving the Multiplicity of High-Spin Crossover States in Transition Metal Iron Complexes, *J. Am. Chem. Soc.*, 2024, **146**(13), 9347–9355, DOI: 10.1021/jacs.4c01637.

22 I. H. M. Van Stokkum, D. S. Larsen and R. Van Grondelle, Global and Target Analysis of Time-Resolved Spectra, *Biochim. Biophys. Acta, Bioenerg.*, 2004, **1657**(2–3), 82–104, DOI: 10.1016/j.bbabio.2004.04.011.

23 I. H. M. Van Stokkum, J. Weißenborn, S. Weigand and J. J. Snellenburg, Pyglotaran: A Lego-like Python Framework for Global and Target Analysis of Time-Resolved Spectra, *Photochem. Photobiol. Sci.*, 2023, **22**(10), 2413–2431, DOI: 10.1007/s43630-023-00460-y.

24 K. Kunnus, M. Vacher, T. C. B. Harlang, K. S. Kjær, K. Haldrup, E. Biasin, T. B. Van Driel, M. Pápai, P. Chabera, Y. Liu, H. Tatsuno, C. Timm, E. Källman, M. Delcey, R. W. Hartsock, M. E. Reinhard, S. Koroidov, M. G. Laursen, F. B. Hansen, P. Vester, M. Christensen, L. Sandberg, Z. Németh, D. S. Szemes, É. Bajnóczi, R. Alonso-Mori, J. M. Glownia, S. Nelson, M. Sikorski, D. Sokaras, H. T. Lemke, S. E. Canton, K. B. Møller, M. M. Nielsen, G. Vankó, K. Wärnmark, V. Sundström, P. Persson, M. Lundberg, J. Uhlig and K. J. Gaffney, Vibrational Wavepacket Dynamics in Fe Carbene Photosensitizer Determined with Femtosecond X-Ray Emission and Scattering, *Nat. Commun.*, 2020, **11**, 634, DOI: 10.1038/s41467-020-14468-w.

25 F. Hainer, N. Alagna, A. Reddy Marri, T. J. Penfold, P. C. Gros, S. Haacke and T. Buckup, Vibrational Coherence Spectroscopy Identifies Ultrafast Branching in an Iron(II) Sensitizer, *J. Phys. Chem. Lett.*, 2021, **12**(35), 8560–8565, DOI: 10.1021/acs.jpclett.1c01580.

26 A. M. Brown, C. E. McCusker and J. K. McCusker, Spectroelectrochemical Identification of Charge-Transfer Excited States in Transition Metal-Based Polypyridyl Complexes, *Dalton Trans.*, 2014, **43**(47), 17635–17646, DOI: 10.1039/C4DT02849J.

27 A. Soupart, F. Alary, J.-L. Heully and I. M. Dixon, On the Possible Coordination on a 3MC State Itself? Mechanistic Investigation Using DFT-Based Methods, *Inorganics*, 2020, **8**(2), 15, DOI: 10.3390/inorganics8020015.

28 C. Daniel and C. Gourlaouen, Chemical Bonding Alteration upon Electronic Excitation in Transition Metal Complexes, *Coord. Chem. Rev.*, 2017, **344**, 131–149, DOI: 10.1016/j.ccr.2016.10.010.

29 C. E. Welby, C. R. Rice and P. I. P. Elliott, Unambiguous Characterization of a Photoreactive Ligand–Loss Intermediate, *Angew. Chem., Int. Ed.*, 2013, **52**(41), 10826–10829, DOI: 10.1002/anie.201304219.

30 L. Salassa, C. Garino, G. Salassa, C. Nervi, R. Gobetto, C. Lamberti, D. Gianolio, R. Bizzarri and P. J. Sadler, Ligand-Selective Photodissociation from $[Ru(Bpy)(4AP)_4]^{2+}$: A Spectroscopic and Computational Study, *Inorg. Chem.*, 2009, **48**(4), 1469–1481, DOI: 10.1021/ic8015436.

31 J. T. Yarranton and J. K. McCusker, Ligand-Field Spectroscopy of Co(III) Complexes and the Development of a Spectrochemical Series for Low-Spin d^6Charge-Transfer Chromophores, *J. Am. Chem. Soc.*, 2022, **144**(27), 12488–12500, DOI: 10.1021/jacs.2c04945.

32 S. Kaufhold, N. W. Rosemann, P. Chábera, L. Lindh, I. Bolaño Losada, J. Uhlig, T. Pascher, D. Strand, K. Wärnmark, A. Yartsev and P. Persson, Microsecond Photoluminescence and Photoreactivity of a Metal-Centered Excited State in a Hexacarbene–Co(III) Complex, *J. Am. Chem. Soc.*, 2021, **143**(3), 1307–1312, DOI: 10.1021/jacs.0c12151.

33 K. Witas, S. S. Nair, T. Maisuradze, L. Zedler, H. Schmidt, P. Garcia-Porta, A. S. J. Rein, T. Bolter, S. Rau, S. Kupfer, B. Dietzek-Ivanšić and D. U. Sorsche, Beyond the First Coordination Sphere-Manipulating the Excited-State Landscape in Iron(II) Chromophores with Protons, *J. Am. Chem. Soc.*, 2024, **146**(29), 19710–19719, DOI: 10.1021/jacs.4c00552.

34 J. Steube, A. Kruse, O. S. Bokareva, T. Reuter, S. Demeshko, R. Schoch, M. A. Argüello Cordero, A. Krishna, S. Hohloch, F. Meyer, K. Heinze, O. Kühn, S. Lochbrunner and M. Bauer, Janus-Type Emission from a Cyclometalated Iron

(III) Complex, *Nat. Chem.*, 2023, **15**(4), 468–474, DOI: 10.1038/s41557-023-01137-w.

35 M. Darari, A. Francés-Monerris, B. Marekha, A. Doudouh, E. Wenger, A. Monari, S. Haacke and P. C. Gros, Towards Iron(II) Complexes with Octahedral Geometry: Synthesis, Structure and Photophysical Properties, *Molecules*, 2020, **25**(24), 5991, DOI: 10.3390/molecules25245991.

36 A. Francés–Monerris, P. C. Gros, X. Assfeld, A. Monari and M. Pastore, Toward Luminescent Iron Complexes: Unravelling the Photophysics by Computing Potential Energy Surfaces, *ChemPhotoChem*, 2019, **3**(9), 666–683, DOI: 10.1002/cptc.201900100.

37 K. Magra, M. Darari, E. Domenichini, A. Francés-Monerris, C. Cebrián, M. Beley, M. Pastore, A. Monari, X. Assfeld, S. Haacke and P. C. Gros, Photophysical Investigation of Iron(II) Complexes Bearing Bidentate Annulated Isomeric Pyridine-NHC Ligands, *J. Phys. Chem. C*, 2020, **124**(34), 18379–18389, DOI: 10.1021/acs.jpcc.0c03638.

38 J. P. Zobel and L. González, The Quest to Simulate Excited-State Dynamics of Transition Metal Complexes, *JACS Au*, 2021, **1**(8), 1116–1140, DOI: 10.1021/jacsau.1c00252.

39 K. Witas, S. S. Nair, T. Maisuradze, L. Zedler, H. Schmidt, P. Garcia-Porta, A. S. J. Rein, T. Bolter, S. Rau, S. Kupfer, B. Dietzek-Ivanšić and D. U. Sorsche, Beyond the First Coordination Sphere-Manipulating the Excited-State Landscape in Iron(II) Chromophores with Protons, *J. Am. Chem. Soc.*, 2024, **146**(29), 19710–19719, DOI: 10.1021/jacs.4c00552.

40 S. Stoll and A. Schweiger, EasySpin, a Comprehensive Software Package for Spectral Simulation and Analysis in EPR, *J. Magn. Reson.*, 2006, **178**(1), 42–55, DOI: 10.1016/j.jmr.2005.08.013.